Colloid and Polymer Science (2020) 298:21–33
https://doi.org/10.1007/s00396-019-04579-2

ORIGINAL CONTRIBUTION

The effects of grafting density and charge fraction on the properties of ring polyelectrolyte brushes: a molecular dynamics simulation study

Qing-Hai Hao[1] · Li-Xiang Liu[1] · Gang Xia[1] · Li-Yan Liu[1] · Bing Miao[2]

Received: 18 July 2019 / Revised: 20 October 2019 / Accepted: 21 October 2019 / Published online: 9 November 2019

Abstract

Using molecular dynamics simulations, the flexible ring polyelectrolyte chains tethered to a planar substrate and immersed in good solvents are investigated systematically. Two sets of simulations are performed to explore the effects of grafting density and charge fraction, respectively. Both the monovalent and trivalent counterions are considered. The height of the brush H follows a scaling relation with grafting density ($\sim\sigma_g^{\nu}$) and charge fraction ($\sim f^{\nu}$). The values of the exponents are different from those of the linear counterparts. Through a careful analysis on the distributions of monomers and counterions, pair correlation functions of monomer-monomer and monomer-counterion, as well as the fractions of trivalent counterions in four states, the equilibrium structures of the ring PE brushes are examined in detail. Furthermore, a brief comparison with the 'equivalent' linear brush is carried out. Also, our results can serve as a guide for improving the performance of ring polyelectrolyte brushes as unique surface modifiers.

Keywords Molecular dynamics simulation · Ring polyelectrolyte brushes · Grafting density · Charge fraction

Introduction

Tethering of polyelectrolyte (PE) chains to the planar or curved surface can yield PE brush, which is considered as one of the most promising approaches for tuning surface properties [1–3]. Indeed, PE brushes are important in a variety of application fields, such as colloid stabilization [4], drug delivery [5], lubrication [6], and stimuli-responsive surfaces [1]. Particular interests focused on the structural and dynamic properties of brushes formed by linear PE chains in the past decades. PE brushes with nonlinear molecular architectures (comb-like, star-like, branched, and ring polymers) have been addressed only recently, and studies in this field are still in progress. Among these nonlinear topologies, ring (non-catenated) polymers, due to the intrinsic absence of chain ends, have been shown to demonstrate unique physical characteristics and remarkable performances compared to their linear counterparts [7]. Understanding the topological effects of ring PE brushes would pave the way for the development of new strategies for surface protecting and open up unrevealed opportunities in material science.

In contrast to the most commonly explored linear PE brushes, only a few theoretical [8–10], experimental [11–16], and simulation [17–26] studies of ring brushes have been reported to date. Most of them focused on the brushes formed by uncharged ring polymers. For example, Cao et al. [8] investigated the surface forces between telechelic polymer coating substrates by employing a polymer density functional theory (PDFT). It was reported that linear and ring brushes exhibited a similar scaling behavior for the brush thickness; however, a significant difference was observed in terms of the brush morphology, especially for the segment densities close to the brush edge. By means of the analytical self-consistent field (ASCF) approach, Borisov and co-workers [9] investigated the structure and lubricating properties of polymer brushes formed by a neutral intra-molecular macrocycle with an equal long linear fragment grafted to a planar surface at

✉ Qing-Hai Hao
qhhao@cauc.edu.cn

✉ Bing Miao
bmiao@ucas.ac.cn

[1] College of Science, Civil Aviation University of China, Tianjin 300300, China

[2] Center of Materials Science and Optoelectronics Engineering, College of Materials Science and Opto-Electronic Technology, University of Chinese Academy of Sciences, Beijing 100049, China

implicit and good solvent conditions. It was predicted that the cyclization-induced weaker interpenetration of sliding brushes might enhance their performance as lubricants, which has been confirmed by molecular dynamics (MD) simulations of ring polymer brushes [17]. Very recently, using lattice self-consistent field (LSCF) calculations, Qiu et al. [10] reported the first systematic study of planar ring homopolymer brushes immersed in an explicit and athermal solvent. Their results clearly shown that ring brushes were nearly, but not completely, identical to the 'equivalent' (half the chain length and double the grafting density) linear brushes. However, for two identical and opposing brushes, ring brushes usually had smaller interpenetration thickness than the equivalent linear analogs.

Experimentally, using a simple drop coating method, Li et al. [11] reported the preparation of planar surfaces bearing loop and linear triblock copolymer chains. The results from quartz crystal microbalance with dissipation (QCM-D) protein adsorption experiments demonstrated that the loop brushes exhibited a more enhanced antifouling performance over the linear counterparts with similar grafting density. Yu and coworkers [12] compared physical properties and bio-interfacial behaviors of gold surfaces tethered cyclic polystyrene brushes with those of the linear polystyrene brushes. It was observed that the denser and more compact ring brushes facilitated absorption of larger proteins while suppressed adsorption of smaller ones. Recently, Benetti and coworkers synthesized a series of ring brushes by the 'grafting-to' technique, such as one poly-2-ethyl-2-oxazoline (PEOXA) on titanium oxide (TiO_2) surfaces [13, 14], different mixtures of loops and linear tails, ring PEOXA brushes on TiO_2 surfaces [15], as well as PEOXA ring brushes on oleic acid-stabilized Fe_3O_4 nanoparticles [16]. As shown in their review paper [7], compared to the linear brushes, ring brushes exhibited a higher repulsive force against compression, reduced the amount of physically absorbed proteins, and enhanced the steric stabilization.

On the other hand, simulations of the unique properties of neutral ring brushes have been recently highlighted. For instance, using MD and Monte Carlo (MC) off-lattice models, Binder and coworkers [18, 19] first investigated the anomalous structure and the chain dynamics in neutral ring (non-catenated) brushes and compared results with those of the 'equivalent' linear brushes. Milchev and Binder [20] studied the adsorption of oligomers and linear flexible macromolecules into a planar brush formed from neutral ring polymers by MC simulations. It was reported that the concentration profiles of oligomers and linear polymers in ring brushes demonstrated little difference from those in the linear brushes. Wu and coworkers [21] investigated the static and dynamic properties of neutral ring polymer chains tethered to a flat substrate at various grafting densities and chain lengths in good solvents by MD simulations. In a following paper, they extended the MD simulations to the planar brushes formed by multi-cyclic chains where each chain consisted of a sequence of small identical rings [22]. Employing non-equilibrium MD simulations, Erbas and Paturej studied [17] the friction between uncharged ring polymer brush bilayers sliding through each other in an implicit and good solvent. They pointed out that both the friction force and the normal pressure of ring brushes were nearly half of those of the 'equivalent' linear counterparts. Very recently, Liu and coworkers [23] presented a simulation study on the nonwettability of a flat surface grafted with neutral loop polymer chain. Both the monodispersed loops (loops with the same length) and polydispersed loops (loops with different lengths) were considered, which were helpful to enhance the nonwettability of the surface. Additionally, Spontak et al. [24–26] conducted a series of simulation works to investigate the properties of double tethered neutral macromolecules to an impenetrable surface, which demonstrated similar loop topology with the ring brushes. The effects of grafting density and chain length on the static conformational properties and dynamic relaxation behaviors under good solvent condition were analyzed. It was reported that the existence of a second grafting point generated little influence on the segments near the chain origin, but promoted the overall coil localization close to the interface.

Ring PE chains, such as synthetic polymers and biopolymers, are common. However, less attention has been paid on the ring PE brushes up to the present. Fabricated by means of an intermediate azide-bearing monolayer, the lubricating properties of surface grafted positively charged polysaccharides were investigated by colloidal probe lateral force microscopy [27]. It was suggested that the complex loop-train-tail structure significantly enhanced the load-bearing properties of the dextran film. Noting that, for charged tethered ring chains, the topological effects by cyclic charged macromolecules would broaden the tuning potential of the interfacial properties, which might be a dominant factor in the reduction of frictional forces and the enhancement of surface antifouling. In this work, we present the first systematic study of non-catenated ring PE brushes grafted on a flat surface and immersed in an implicit and good solvent by means of MD simulations. The effects of grafting density, counterion valence, as well as charge fraction on the equilibrium structures of the ring PE brushes are examined in detail. Our theoretical work helps to reveal the unique physical-chemical properties of ring PE brushes originated from the long-range Coulomb interactions.

Simulation details

Simulations of planar ring PE brushes are performed using coarse-grained Kremer-Grest bead-spring model [28]. Three basic units, length σ, mass m, and energy ε, are employed in our simulations. Other units are derived from these basic ones. The PE chain is modeled as a ring formed by N_R connective

beads with diameter σ. The ring chains are anchored to a flat neutral substrate to form a regular 6 × 6 square grid. Each charged segment of ring PE chain carries a negative electrical charge $-e$. Positive charged counterions (monovalent or trivalent) are added to a simulation box for keeping electroneutrality. The simulation box has dimensions $L_x \times L_y \times L_z$, where $L_z = 150$ is fixed during our simulations. L_x and L_y are adjusted to fulfill our desired grafting density $\sigma_g = 36/L_xL_y$. The grafting surface is located at $z = 0$. A nonselective and impenetrable surface is located at $z = L_z$ to prevent counterions from escaping. Periodic boundary conditions are enforced in the x and y directions.

The pairwise excluded volume interactions between any two beads are modeled by a truncated-shifted Lennard-Jones (LJ) potential

$$U_{\mathrm{LJ}}(r) = \begin{cases} 4\varepsilon\left[\left(\frac{\sigma}{r}\right)^{12} - \left(\frac{\sigma}{r}\right)^{6} - \left(\frac{\sigma}{r_c}\right)^{12} + \left(\frac{\sigma}{r_c}\right)^{6}\right] & r \le r_{\mathrm{c}} \\ 0 & r > r_{\mathrm{c}} \end{cases} \quad (1)$$

where r is the distance of any two beads. $\varepsilon = 1.0k_{\mathrm{B}}\mathrm{T}$ (k_B is the Boltzmann constant and T is the absolute temperature) is the interaction strength regardless of bead type. The cutoff distance $r_c = 2^{1/6}$ is the same for all the pairwise interactions. The choices of parameters of ε and r_c correspond to good solvent conditions for the polymer backbone.

The bonds are maintained by the finite extension nonlinear elastic (FENE) potential [28]

$$U_{FENE}(r) = -\frac{1}{2}k_{spring}R_{\max}^2 \ln\left[1 - \left(\frac{r}{R_{\max}}\right)^2\right] \quad (2)$$

where $k_{\mathrm{spring}} = 30.0\varepsilon/\sigma$ and $R_{\max} = 1.5\sigma$ are the spring constant and the maximum bond length, respectively. This attractive FENE potential coupled with the excluded volume interaction (LJ potential) can prevent the bonds to penetrate each other. Moreover, whether the ring topology is conserved during the whole simulation process is crucial for our simulation results. Besides the FENE potential of the ring chains, we also monitor the topological information of the tethered ring PE chains. Once a bond length exceeds the maximum length or the ring topology is not conserved during the run, the simulation process will be interrupted immediately. Furthermore, the time step size is chosen rationally to ensure the ring topology conserved throughout the simulation on the basis of existing simulation literature [28].

The Coulomb potential is employed to describe the electrostatic interactions between charged beads with the charge valences q_i and q_j and separated by the distance r

$$U_{Coul}(r) = k_BT\frac{l_Bq_iq_j}{r} \quad (3)$$

where l_B is the Bjerrum length $l_B = e^2/\varepsilon_0\varepsilon_r k_BT$ (ε_0 and ε_r are the vacuum permittivity and the relative dielectric constant of the implicit solvent). Note that the Bjerrum length in solutions is about 2~5 times of distance between charged residues along polymer backbone for many synthetic PEs and biomacromolecules [29], we select a typical value $l_B = 3\sigma$, which has been widely used in the literatures [30–32]. The long-range part of the Coulomb potential is calculated by means of the particle-particle particle-mesh (PPPM) algorithm [33]. To calculate the electrostatic interaction of the 2D periodic system, an empty volume with thickness of $3L_z$ is inserted along z-direction [34].

MD simulations are carried out in a canonical ensemble (constant number of beads N, volume V, and temperature T) using the open-source software LAMMPS [35]. The constant temperature is maintained by coupling the system to a Langevin thermostat [33, 35]. The motion of any bead i is governed by the Langevin equation

$$m\frac{d^2r_i(t)}{dt^2} = F_i - \xi\frac{dr_i(t)}{dt} + F_i^R(t) \quad (4)$$

where the mass $m = 1.0$ is identical for all types of beads. $\mathbf{F}_i$ is the total deterministic force of other beads interacted with the ith beads. $\xi = 0.143m/\tau$ ($\tau = (m\sigma^2/\varepsilon)^{1/2}$ is the standard LJ time unit) is the friction coefficient. $\mathbf{F}_i^{\mathrm{R}}(t)$ is the random force of the ith bead, which is related to the friction coefficient ξ by the fluctuation-dissipation theorem $\langle\mathbf{F}_i^{\mathrm{R}}(t)\cdot\mathbf{F}_j^{\mathrm{R}}(t')\rangle = 6mk_{\mathrm{B}}T\delta_{ij}\delta(t-t')$. The temperature is set as $T = 1.0$. The velocity Verlet algorithm with a time step $\Delta t = 0.005\tau$ is employed to integrate the equations of motion, which is reasonable for the coarse-grained model of polymer brushes [28, 36, 37]. Initially, the PE chains, in extended configurations, are perpendicular to the tethered surface. Monovalent or trivalent counterions are homogeneously dispersed in the simulation box. The system is equilibrated for 3×10^6 time steps. Two operations are employed to ensure that the system reaches the equilibrium state. On one side, during the equilibration run, we monitor the time evolutions of the thermodynamic quantities (temperature, energy, and pressure) as well as the structural parameters (brush height and radius of gyration) to ensure that the parameters have reached a steady-state regime. On the other side, the autocorrelation function $C_H(t)$ of the brush height is calculated, which can be defined as [38]

$$C_H(t) = \frac{\langle\delta H(t)\delta H(0)\rangle}{\langle H^2\rangle - \langle H\rangle^2}, \delta H(t) = H(t) - \langle H\rangle \quad (5)$$

where H refers to the brush height and is defined in Equation 6. For clarity, the $C_H(t)$ of the two typical grafting densities (σ_g = 0.0025, 0.1) with different charge fractions in the presence of monovalent and trivalent counterions are plotted in Fig. 1.

As depicted in Fig. 1, all the autocorrelation functions decay to zero at $t < 500\tau$ (10^4 time steps), which is much shorter

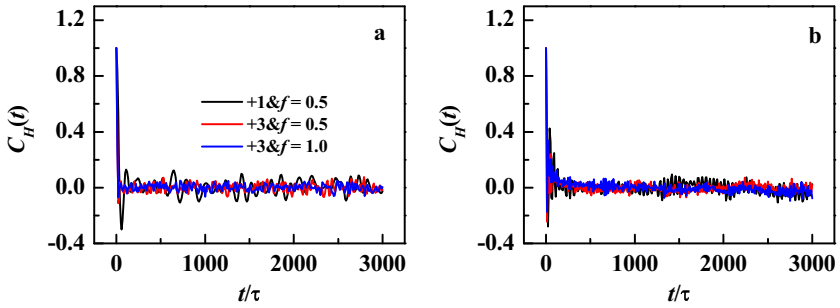

Fig. 1 Autocorrelation function of the height of ring PE brush with different charge fractions in the presence of monovalent and trivalent counterions. **a** σ_g = 0.0025, **b** σ_g = 0.1

than the time of the equilibrated run (3×10^6 time steps). Therefore, it is acceptable that the system is not in kinetical trap state [39]. Then, a production run is performed for 4×10^6 time steps. A snapshot from simulations is saved every 2×10^3 time steps and 2001 configurations are collected for analyzing the properties of ring brushes by our programs.

Results and discussions

The effect of grafting density

Grafting density is one of the most important parameters that could be controlled during the ring PE brush synthesis process [7]. Firstly, the effect of grafting density on the equilibrium structures of the ring PE brush is characterized by the height of the brush, which can be defined as

$$H = \frac{2\int_0^{L_z} z\rho_m(z)dz}{\int_0^{L_z} \rho_m(z)dz} \quad (6)$$

where $\rho_m(z)$ is the distributions of the monomers along the z-axis direction. And the mean-square radius of gyration in the z-direction perpendicular to the grafting surface can also be calculated by

$$R_{gz} = \frac{1}{N}\sum_{i=1}^{N}\left\langle (z_i - z_{cm})^2 \right\rangle^{1/2} = \frac{1}{N^2}\sum_{i=1}^{N}\sum_{j=1}^{N}\left\langle (z_i - z_j)^2 \right\rangle^{1/2} \quad (7)$$

where z_i is the z-component of the ith monomer position vector and z_{cm} refers to the center of mass of the tethered PE chains along the z-direction. The ring PE brush height and the radius of gyration in the z-direction as a function of the grafting density are plotted in Fig. 2 a and b.

At low grafting densities of $\sigma_g < 0.01$, the distance between grafting points of ring chains is large enough that the brush layer consists of individual chains, which is in the so-called 'mushroom' regime with monovalent counterions. The brush height and the z-component of radius of gyration are almost constant in the presence of monovalent counterions (see filled squares in Fig. 2a, b). However, they show a slight decrease with increasing the grafting density in the presence of the trivalent counterions (see filled circles, upper, and down triangles in Fig. 2a, b). The conformations of individual chains in a mushroom regime are determined by intra-chain electrostatic interactions, which will be analyzed in Fig. 6. Trivalent

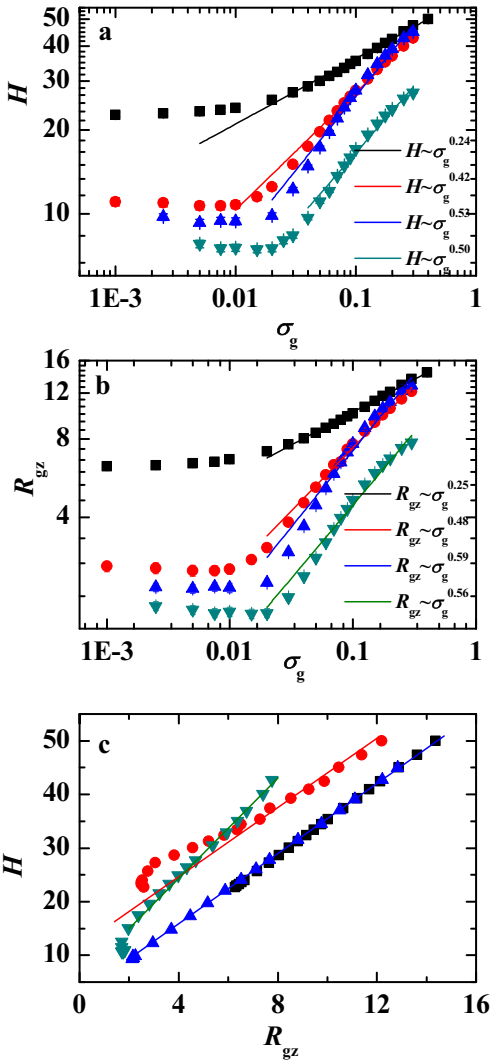

Fig. 2 The heights of the ring PE brushes (**a**) and the z-component of the radius of gyration (**b**) as a function of the grafting density. **c** Replot of H versus R_{gz} at different grafting densities. The filled square denotes the case of chain length N_R = 100 and charge fraction f = 0.5 with monovalent counterions. The filled circle represents the case of N_R = 100 and f = 0.5 with trivalent counterions. The filled upper triangle indicates the case of N_R = 100 and f = 1.0 with trivalent counterions. The filled down triangle indicates the case of N_R = 60 and f = 1.0 with trivalent counterions

counterions can induce the grafted ring PE chains to shrink, which is mainly due to the deduction of osmotic pressure arising from the replacement of monovalent counterions by trivalent ions and the so called 'bridging' mechanism (the ability of one trivalent ion to binding three charged segments). The multivalent ion induced brush collapse was also observed in the linear PE brushes [30, 40].

With increasing the grafting density, a crossover from 'mushroom' regime to 'brush' regime occurs. One can expect that the height of brush and the z-component radius of gyration will increase with the increase of the grafting density, and the excluded volume effect becomes important in the brush regime. Wu and coworkers [21] reported that the thickness of neutral ring polymer brushes behaved a scaling law of $H \sim \sigma_g^{0.27}$ in good solvent, rather than $H \sim \sigma_g^{1/3}$ for a linear polymer brush. Furthermore, the strong linear PE brush was found to have the same scaling behavior as the neutral brush in the so-called osmotic brush regime [41]. For $\sigma_g > 0.025$ in the brush regime, the lateral inhomogeneous patterns of the brush layers (see Fig. 4c, e) formed in the low grafting density are broken, uniform layer morphology can be observed, and the scaling exponents are calculated only for these homogenous ring PE brushes. The brush thickness also follows the scaling relationship $H \sim \sigma_g^{\nu}$ in the brush regime. The scaling exponent $\nu = 0.24$ in the presence of monovalent counterions (filled squares in Fig. 2a) is slightly lower than that of the linear PE brush ($\nu = 1/3$). And the value of scaling exponent in the presence of monovalent counterions is close to that of the neutral ring brush ($\nu = 0.27$) predicted by Wu and coworkers [21], which indicates that the electrostatic screening effect of monovalent counterions is pronounced and the ring PE brush behaves like a neutral brush. However, the adding of trivalent counterions induces a larger scaling exponent for ring PE brushes. Specifically, the scaling exponent increases with the charge fraction for fixed chain length $N_R = 100$, that is, $\nu = 0.53$ for $f = 1.0$ (filled circles in Fig. 2a) and $\nu = 0.42$ for $f = 0.5$ (filled upper triangles in Fig. 2a). We can understand this feature by analyzing the bridging effect of trivalent counterions. The ring chains are inclined to form the pinned-micelle structures induced by the strong electrostatic absorption of trivalent counterions to the charged residues. The micelle-like structures aggregate more tightly with the increase of charge fraction, which yields to a lower brush height for high charge fraction in the low grafting densities. The evolution of brush height with grafting density corresponds to a larger scaling exponent for the high charge fraction in the presence of trivalent counterions for the high grafting density conditions. The scaling exponent $\nu = 0.50$ for $N_R = 60$ (see filled down triangles in Fig. 2a) is slightly lower than that of $N_R = 100$ for fixed $f = 1.0$. As shown in Fig. 2b, the z-component of radius of gyration demonstrates a similar power laws $R_{gz} \sim \sigma_g^{\nu}$ to that of the brush height.

According to the 'Alexander picture' [42] of a neutral polymer brush, one can conclude that $H \propto R_{gz}$ under good solvent conditions. For the ring PE brushes, we re-plot H vs. R_{gz}, focusing on the effects of grafting density at fixed chain length and charge fraction of tethered ring PE chains, which is shown in Fig. 2c. It is observed that the height of the ring PE brushes exhibits a linear profile with R_{gz}, which is similar to the linear polymer brushes. Furthermore, the slope of the linear profile can be affected by the chain length, which is irrespective to the counterion valence and charge fraction of the ring backbone.

The distribution profile of monomers as well as counterions in the z-direction perpendicular to the grafting surface is one of the central properties of the ring PE brush. Based on the MD trajectory data, the distribution profiles of monomers and counterions along z-axis are calculated. Two series of typical distribution profiles are plotted in Fig. 3, namely, one is $\sigma_g = 0.0025$ (the mushroom regime and see Fig. 3a, b), and the other is $\sigma_g = 0.1$ (the brush regime and see Fig. 3c, d), respectively. In the case of low grafting density, a pronounced peak profile is observed in the presence of trivalent counterions regardless of charge fraction (red and blue curves in Fig. 3a), which corresponds to collapsed mushroom morphology induced by the 'bridging' mechanism of multivalent ions. Also, the width of the main peak becomes slightly narrower with the increase of charge fraction, which coincides with the evolution of the brush height with charge fraction in the low grafting densities shown in Fig. 2a. In the case of monovalent counterions, the electrostatic correlation effect is absent and the ring PE brush adopts a relative more swollen structure due to the hydrophilic solvents (black curve in Fig. 3a). As shown in Fig. 3b, almost all trivalent counterions are confined in the brushes because of the strong attraction between charged residues and trivalent ions, which is also evidenced by the low value of fractions of free trivalent counterions shown in Fig. 6a. However, part of monovalent counterions can move outside of the brush due to the translational entropy of counterions. In the case of the brush regime, the ring PE brushes are in a stretched state because of the excluded volume effect originated from the high grafting density, which is more pronounced in the presence of monovalent counterions (see Fig. 3c). An oscillated profile especially for the monovalent case can be observed for small z region, which can be attributed to the excluded volume effect of grafting surface. Furthermore, the variation of $\rho_m(z)$ near the brush periphery in the trivalent counterions is steeper than that of the monovalent counterions, which is beyond the strong stretching limit of the self-consistent field theory $\rho_m(z) = 1-(z/H)^2$ [43, 44]. As one can expect, the distribution profiles of counterions in the brush regime (see Fig. 3d) resemble the profiles of the monomers (see Fig. 3c).

In order to investigate the lateral phase separation of ring PE brushes induced by the trivalent counterions at low grafting densities, we calculate the distributions of time-averaged monomer (left panels) and counterion (right panels)

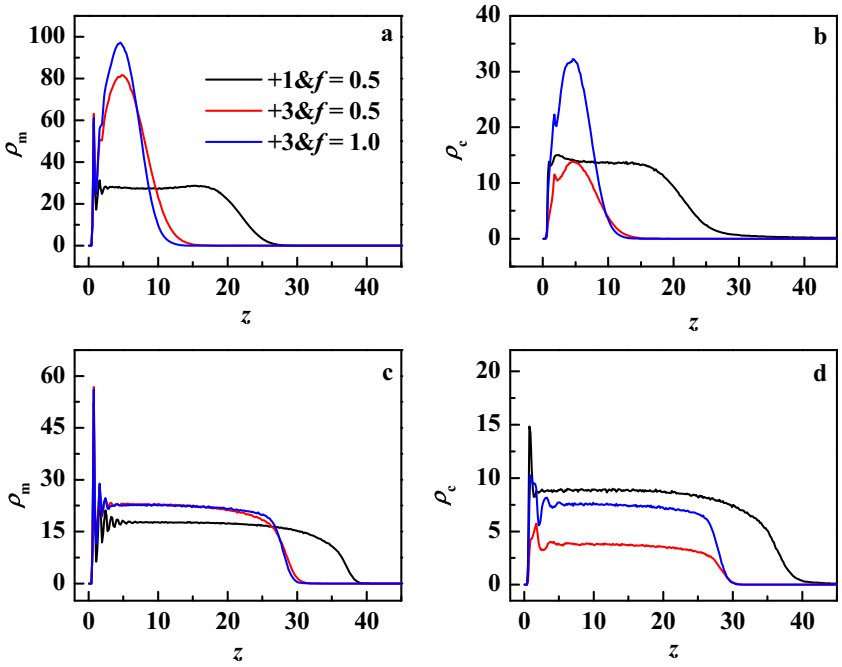

Fig. 3 Monomer and counterion distributions versus distance from the substrate for the low grafting density $\sigma_g = 0.0025$ (upper panels) and high grafting density $\sigma_g = 0.1$ (lower panels) for the chain length $N_R = 100$

density projected onto the *xy* plane (a top-down view), which are plotted in Fig. 4. Only the cases of charge fraction $f = 1.0$ and chain length $N_R = 100$ are provided, which corresponds to the solid upper triangles in Fig. 2a. As shown in Fig. 4a, owing to the large distance between neighboring ring chains at $\sigma_g = 0.0025$, the ring PE brush adopts an isolated chain morphology, where the high density points correspond to the grafting sites. With increasing grafting density, the pinned-micelle morphologies are formed at $\sigma_g = 0.005$ (see Fig. 4c) and $\sigma_g = 0.0075$ (see Fig. 4e), that is, a number of ring PE chains aggregate together to form a micelle, where the chains are still tethered onto the substrate (referred as 'legs'). Furthermore, the characteristic size of the heterogeneous pattern gets larger with increasing grafting density. These lateral phase separation structures induced by multivalent ions under good solvent conditions have also been reported for the linear PE brushes [30, 45–47]. For further increasing the grafting density, the lateral heterogeneous pattern disappears, that is, system forms the uniform layer morphology in the brush regime. Because of the strong electrostatic attraction between polyions and trivalent counterions, almost all trivalent counterions are condensed onto the polymer backbone, which leads to the similar lateral distributions (right panels) with those of monomers for fixed grafting density.

In order to illustrate the correlation effect of trivalent counterions on the properties of the ring PE brushes, we further calculate the fractions of free (ψ_{free}), nearest neighbor condensation (ψ_{NNC}), intra-chain bridging (ψ_{IAB}), and inter-chain bridging (ψ_{IEB}) trivalent counterions as a function of grafting density, which has been demonstrated schematically in Fig. 5. Specifically, the cutoff distance $R_c = 2^{1/6}$ (marked with a dash circle in Fig. 5) is taken for constructing the neighbor list of each trivalent counterion, which corresponds to the cutoff distance of the pairwise interaction between monomers and counterions in good solvents.

The dependence of fractions of trivalent counterions on the grafting density is plotted in Fig. 6 for different chain lengths. Specifically, the competition between the translational entropy of counterions and the charged residue-counterion electrostatic attraction determines the free or condensed states of the trivalent counterions. The condensed counterions appear as three states, namely, nearest neighbor condensation, intra-chain bridging, and inter-chain bridging. The role of nearest neighbor condensation counterions is mainly to renormalize the polyion charge to a smaller effective value. The intra-chain and inter-chain bridging counterions induce an effective attractive interaction between polymer segments, manifesting the electrostatic correlation effect.

As shown in Fig. 6a, the fraction of free trivalent counterions is almost constant in $\sigma_g \leq 0.05$, which is independent of the grafting density. Increasing charge fraction from $f = 0.5$ to $f = 1.0$ yields a relative high local charge density of the ring PE brush and drives more trivalent counterions to condense onto the polymer backbone, inducing a smaller value of ψ_{free} for $f = 1.0$ (see the filled circles and triangles in Fig. 6a). Moreover, the value of ψ_{free} is irrespective with the ring chain length. For $\sigma_g > 0.05$, the fractions of free counterions decrease gradually to zero with increasing grafting density. Furthermore, the evolution of ψ_{free} with the grafting density can be understood from the Manning theory [48, 49]. In the Manning theory, the fraction of free counterions ψ_{free} is given as $\psi_{free} = b/(q_c f l_B)$, where $b = 1.0$ is distance of two neighboring

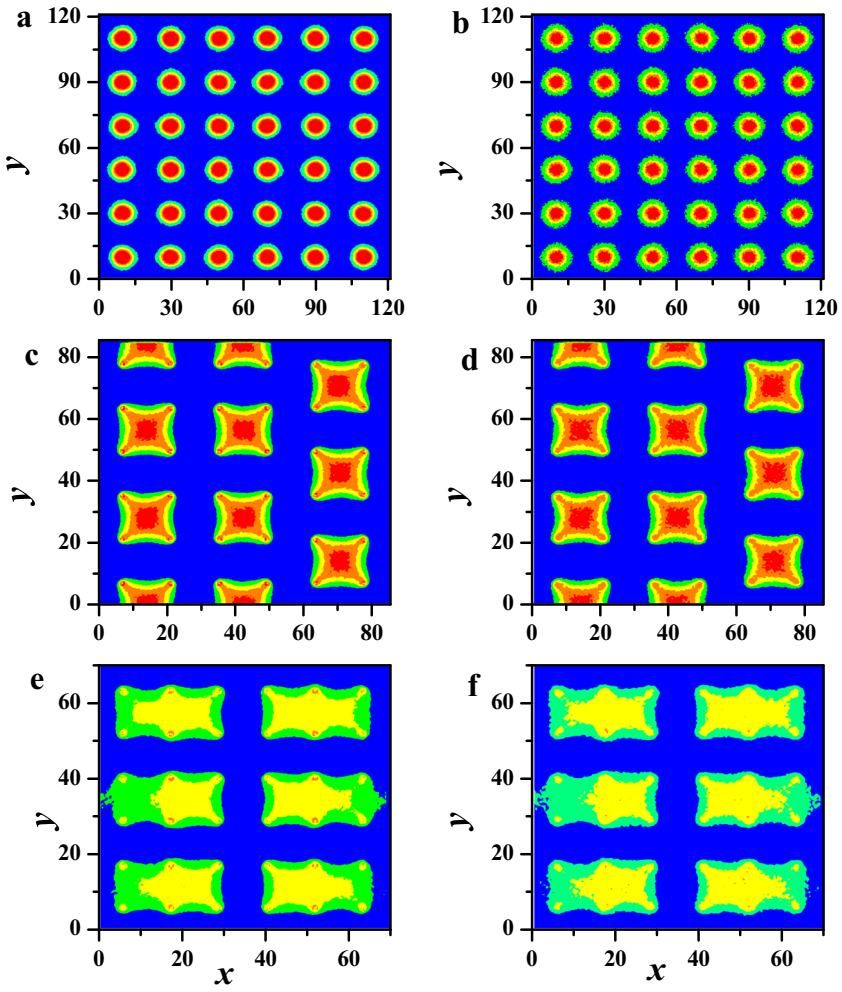

Fig. 4 Top-down view of ring PE brush (left panels) and trivalent counterions (right panels) density profiles for charge fraction $f = 1.0$ and chain length $N_R = 100$ at different grafting densities. **a**, **b** $\sigma_g = 0.0025$, **c**, **d** $\sigma_g = 0.005$, **e**, **f** $\sigma_g = 0.0075$

monomers in one chain and q_c is the counterion valence. Note that $l_B = 3.0$ in our simulations, we find $\psi_{free} = 0.22$ and 0.11 of trivalent counterions according to the Manning theory, which correspond to charge fractions of $f = 0.5$ and $f = 1.0$, respectively. For low grafting densities $\sigma_g \leq 0.05$ shown in Fig. 6a, $\psi_{free} = 0.28$ and 0.13 are observed for $f = 0.5$ (solid squares) and $f = 1.0$ (solid circles and triangles), respectively, which is in good agreement with the Manning theory. For the large grafting densities of $\sigma_g > 0.05$, the ψ_{free} decreases to zero and deviates from the Manning theory, which can be attributed to the fact that Manning's condensation theory is defined for an infinitely long PE chain of rod shape in the infinite-dilute limit.

As depicted in Fig. 6b, almost half of trivalent counterions are in the nearest neighbor condensation state and remain unchanged in $\sigma_g \leq 0.05$, which is regardless of the grafting density and charge fraction. And the value of ψ_{NNC} decreases to zero with increasing the grafting density. For the trivalent counterions in the bridging state, the intra-chain bridging fractions decrease roughly linearly (see Fig. 6c), which leads to a rapid increasing profile of the ψ_{IEB} (see Fig. 6d). The relative high charge density of charged residues in the case of high grafting density promotes one trivalent counterion to bind three charged monomers, which is referred as the electrostatic correlation. And the three monomers belong to different ring PE chains with a high probability, which corresponds to a large value of the inter-chain bridging fraction (see Fig. 6d). Furthermore, the fractions of trivalent counterions in both intra-chain and inter-chain states for $f = 0.5$ are lower than those of $f = 1.0$ for a fixed grafting density.

In order to further investigate the effect of grafting density on the structuring of ring PE brushes, we calculate the pair correlation functions (PCF) of monomer-monomer and monomer-counterion. Only two densities are shown in Fig. 7 for clarity, which correspond to the mushroom regime ($\sigma_g = 0.0025$; Fig. 7a, b) and the brush regime ($\sigma_g = 0.1$; Fig. 7c, d). For the low grafting density, representing the individual mushroom structure, the PCFs of monomer-monomer have a pronounced intra-chain correlation as shown in Fig. 7a. The amplitude of the primary peak and the long-range sub-peak becomes larger slightly for high charge fraction and short chain length (the dark cyan curve). Because of the strong

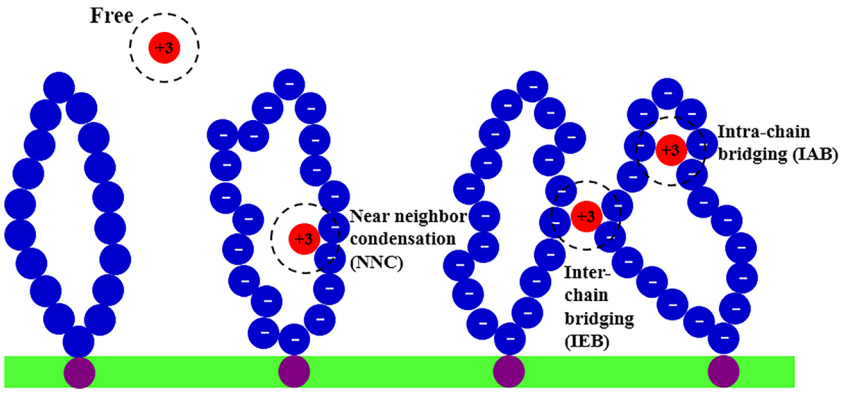

Fig. 5 Schematic for classifying trivalent counterions into four states in the ring PE brush, that is, the free state, the nearest neighbor condensation state, the intra-chain bridging state, and the inter-chain bridging state. The filled green rectangle represents the grafting surface. Purple beads correspond to the grafting points. Blue beads refer to the monomers. Red beads indicate to the trivalent counterions

electrostatic attraction between the charged monomers and trivalent counterions, the PCFs of monomer-counterion demonstrate a more pronounced nearest-neighbor correlation peak than that in the presence of monovalent counterions (see Fig. 7b). Furthermore, the height of the primary peak in $g_{mc}(r)$, located at $r = 1.1$, becomes more pronounced for the high charge fraction and short chain length (the dark cyan curve in Fig. 7b). For the high grafting density $\sigma_g = 0.1$, both the intra-chain correlations in $g_{mm}(r)$ (see Fig. 7c) and the nearest-neighbor correlation in $g_{mc}(r)$ (see Fig. 7d) become weaker compared with those in the low grafting density, which can be understood from the uniform layer structure of the ring PE brushes induced by high tethering density.

The effect of charge fraction

The charge fraction of the grafting PE chains is an important factor to determine the structure of the brushes. In this section, for fixed grafting densities (low grafting density $\sigma_g = 0.0125$ as well as high grafting density $\sigma_g = 0.1$), the effects of charge fraction of tethered ring PE chains with chain length $N_R = 100$ in the presence of monovalent and trivalent counterions are studied. Furthermore, the 'equivalent' linear counterparts of ring PE chains are also considered for comparison. The heights of the brush as a function of charge fraction are displayed in Fig. 8.

As shown in Fig. 8, the height of the ring PE brush is given by $H \sim f^{\nu}$, where f is the charge fraction of the tethered PE chains. In the case of monovalent counterions, the height of the brush increases with the increasing of charge fraction. The exponents $\nu = 0.18$ and 0.16 for the low and high grafting densities, respectively (see the solid squares and circles in Fig. 8), which are almost independent of the grafting density. In the presence of trivalent counterions, the dependence of the height of the ring PE brush on the charge fraction demonstrates distinct scaling relations. Namely, the height of the

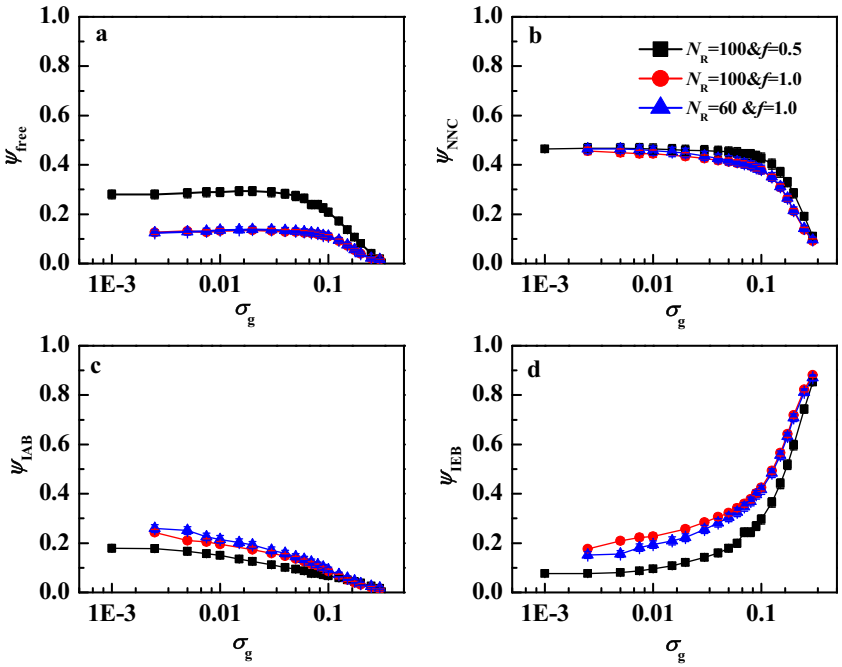

Fig. 6 The fractions of free (**a**), nearest neighbor condensation (**b**), intra-chain bridging (**c**), and inter-chain bridging (**d**) trivalent counterions as a function of grafting density

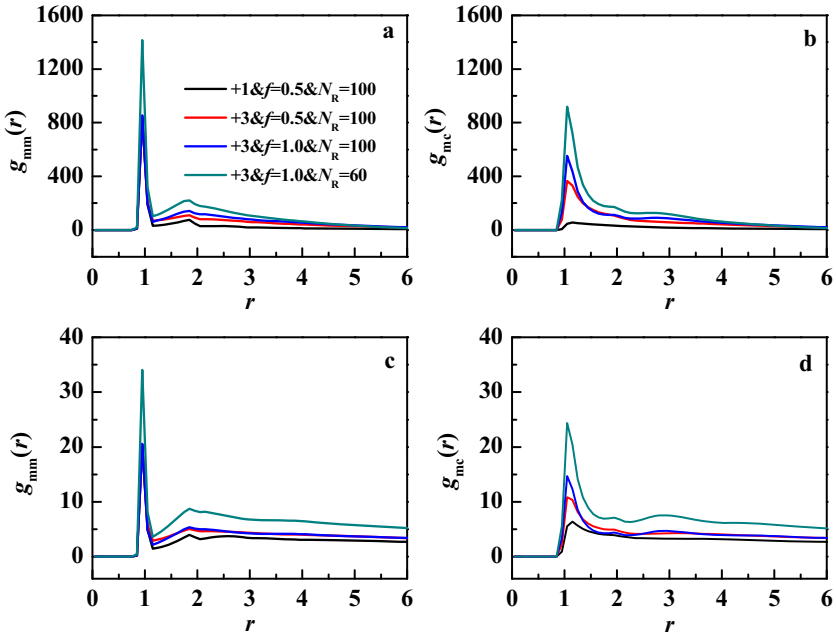

Fig. 7 The pair correlation functions of monomer-monomer $g_{mm}(r)$ and monomer-counterion $g_{mc}(r)$ for the low grafting density $\sigma_g = 0.0025$ (upper panels) and high grafting density $\sigma_g = 0.1$ (lower panels)

brush decreases with the increasing of charge fraction at low grafting density ($\nu = -0.19$ and see filled down triangles in Fig. 8), which can be attributed to the enhancing electrostatic bridging of multivalent ions originated from high charge fraction. Even under good solvent conditions, the effective attraction of polyions originated from electrostatic correlation can lead to a relative compact configuration of the brush with increasing the charge fraction. This collapse of brush induced by enhancing electrostatic correlation in good solvent was also observed in our simulation work of linear spherical PE brushes [31]. Whereas at high grafting density, the excluded volume effect is dominant, the brush exhibits a uniform, extended morphology, and the brush height is almost irrespective with the charge fraction ($\nu = 0.01$). Furthermore, the scaling law of the 'equivalent' linear PE brushes is also depicted in Fig. 8 with open symbols, and the similar scaling fashion can be observed with the corresponding ring PE brushes. According to the predictions of the scaling analysis [41], the brush height scales with the charge fraction as $H \sim f^{1/2}$ in the osmotic brush regime for the linear PE brushes. We observe that the exponent of the ring PE brushes is affected by the grafting density and counterion valence. This is different from the results of the scaling method.

In order to reveal the effect of charge fraction on the ring brush morphologies, the distributions of monomers and counterions along the z-direction are also calculated. For clarity, only two charge fractions are provided in Fig. 9, that is, low charge fraction $f = 0.1$ (left panels) and high charge fraction $f = 1.0$ (right panels). In the cases of low charge fractions, the distributions of monomers are almost identical for high grafting density $\sigma_g = 0.1$ (see red and blue lines in Fig. 9a), which are independent of the counterion valence. This is the

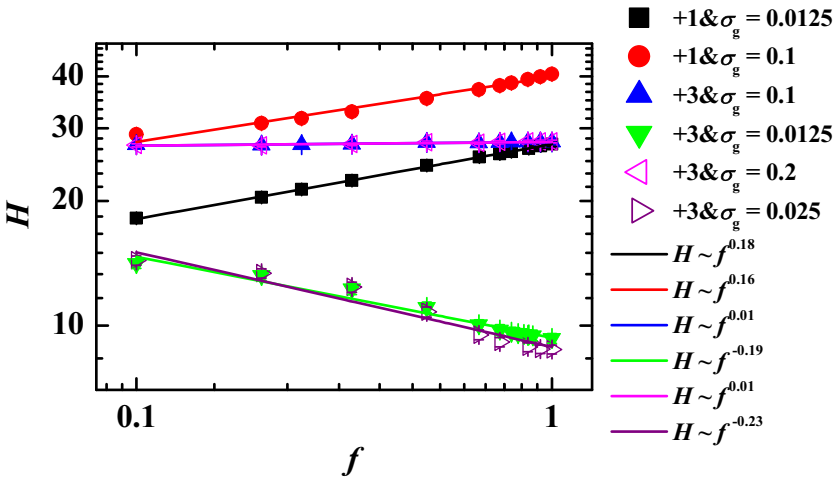

Fig. 8 The heights H of the brushes as a function of charge fraction of tethered chains for ring PE brushes and the linear ones. The filled symbols correspond to the ring PE brushes with the chain length $N_R = 100$. The open symbols represent the linear PE brushes with the chain length $N_L = 50$

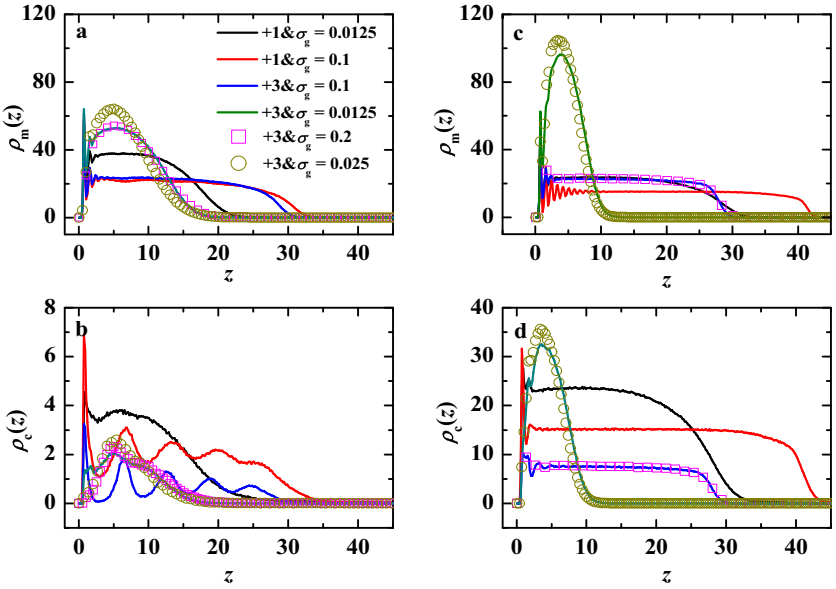

Fig. 9 Monomer and counterion distributions versus distance from the substrate for the low charge fractions $f = 0.1$ (left panels) and high charge fractions $f = 1.0$ (right panels). The lines represent the ring PE brushes with the chain length $N_R = 100$ and the open symbols stand for the linear PE brushes with the chain length $N_L = 50$

representation that the excluded volume interaction induced by high grafting density is dominant compared with the electrostatic interaction of low charge fraction. For the low grafting density $\sigma_g = 0.0125$, the electrostatic screening of monovalent counterions makes the brush in a relative shrunken conformation. Combined with the bridging effect, the collapsed morphology is more pronounced for the system with trivalent counterions (the dark cyan line in Fig. 9a). When the charge fraction increases to $f = 1.0$, the monomers can be distributed in the space far away from the substrate in the presence of monovalent counterions (see black and red lines in Fig. 9b) than those in the low charge fractions. However, the ring PE brush in the trivalent solutions maintains a uniform extended morphology for the high grafting density $\sigma_g = 0.1$ (see blue line in Fig. 9b), which indicates that the excluded volume interaction plays a dominant role compared with the electrostatic correlation mediated by multivalent ions. Whereas in the low grafting density $\sigma_g = 0.0125$, the collapsed brush induced by multivalent ion bridging can be observed (the dark cyan line in Fig. 9b). The variations of distribution of monomers induced by increasing charge fraction are consistent with the height of ring PE brush shown in Fig. 8.

As shown in the lower panels of Fig. 9, the distribution range of counterions is almost coincided with those of charged monomers, which indicates that almost all counterions are confined in the brush layer. Specifically, in the cases of low charge fraction $f = 0.1$, it is worth noting that five peaks are observed in turn along z-direction for the distribution of counterions for $\sigma_g = 0.1$ (red and blue lines in Fig. 9c). The scenario of five peaks can be understood from the distribution of charged residues along the ring chains, that is, there are ten charged segments in one ring chain (chain length $N_R = 100$ and charge fraction $f = 0.1$). The ring topology of tethered chains induces the pair distribution of negative charge of monomers, which corresponds to the five peaks of the distribution profiles of counterions. Furthermore, the distributions of monomers as well as counterions of the 'equivalent' linear chains (open symbols in Fig. 9c) are similar with those of ring chains. In the case of high charge fractions $f = 1.0$ shown in Fig. 9d, the distributions of trivalent counterions demonstrate almost the same profiles with those of monomers plotted in Fig. 9b; however, their magnitudes are one third of those in the monomer distribution profiles, which result from the requirement of electroneutrality.

In order to reveal the influence of charge fraction on the surface morphology of PE brushes, the lateral density distributions of monomers of ring ($\sigma_g = 0.0125$) and linear ($\sigma_g = 0.025$) PE brushes with trivalent counterions are plotted in Fig. 10. Both the low charge fraction $f = 0.1$ (left panels) and the high charge fraction $f = 1.0$ (right panels) are provided. As shown in Fig. 10a, there is not lateral phase separated structures of ring PE brushes at low charge fraction $f = 0.1$; however, the heterogeneous patterns of ring brush layer can be observed at high charge fraction $f = 1.0$ displayed in Fig. 10b, which can be understood from that the increased charge fraction of polyions will promote more trivalent ions to play the intra/inter-chain bridging role in the good solvent. This charge fraction induced lateral phase separated structures in the presence of multivalent ions can also be observed for the linear PE brushes showed in Fig. 10 c and d. Furthermore, the surface patterns of ring PE brush (Fig. 10b) aggregate more tighter than those of its linear counterpart (Fig. 10d), which displays the similar trend for the double tethered neutral polymer brushes [24–26].

In order to further characterize the structure of the ring PE brushes induced by charge fraction, the PCFs of monomer-monomer as well as monomer-counterion are calculated. Similar to Fig. 9, only low charge fraction $f = 0.1$ and high

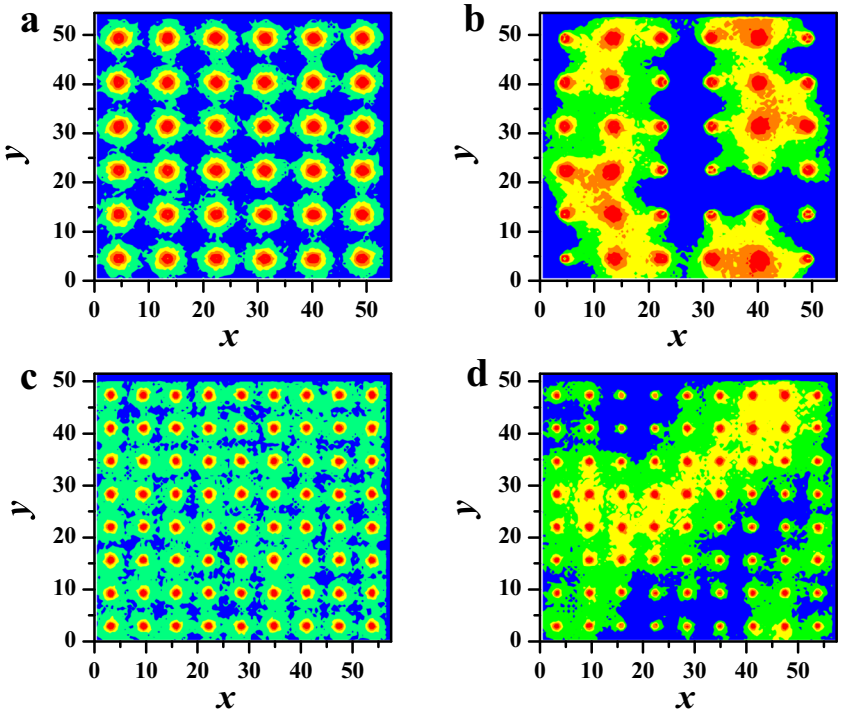

Fig. 10 Upper panels are top-down views of ring PE brush with the chain length N_R = 100 and grafting density σ_g = 0.0125 in the presence of trivalent counterions at different charge fractions, **a** f = 0.1, **b** f = 1.0. Lower panels correspond to top-down views of 'equivalent' linear PE brush with the chain length N_L = 50 and grafting density σ_g = 0.025 in the presence of trivalent counterions at different charge fractions, **c** f = 0.1, **d** f = 1.0

charge fraction f = 1.0 are shown in Fig. 11. The sharp intra-chain correlation peak of $g_{mm}(r)$ is observed for the low grafting densities (see Fig. 11a, b), which is regardless of charge fraction. The inter-chain correlation becomes pronounced when the charge fraction varies from 0.1 to 1.0, especially for the presence of trivalent counterions. The ordered structure induced by multivalent ions was reported by means of experiments and simulations [30–32], which is also observed for our ring PE brushes. For the high grafting densities, both the intra-chain and inter-chain correlations of the monomer-monomer are weaker comparing with those of low grafting densities, which corresponds to the homogeneous layer morphology. As shown in Fig. 11 c and d, an obvious nearest-neighbor correlation peak of $g_{mc}(r)$ is formed in trivalent counterion system for the low grafting densities because of the strong Coulomb attraction between charged residues and multivalent ions. Moreover, the peak is more pronounced with the increase of charge fraction for fixed grafting density. Furthermore, correlations of monomer-monomer as well as monomer-counterion of the 'equivalent' linear PE brushes

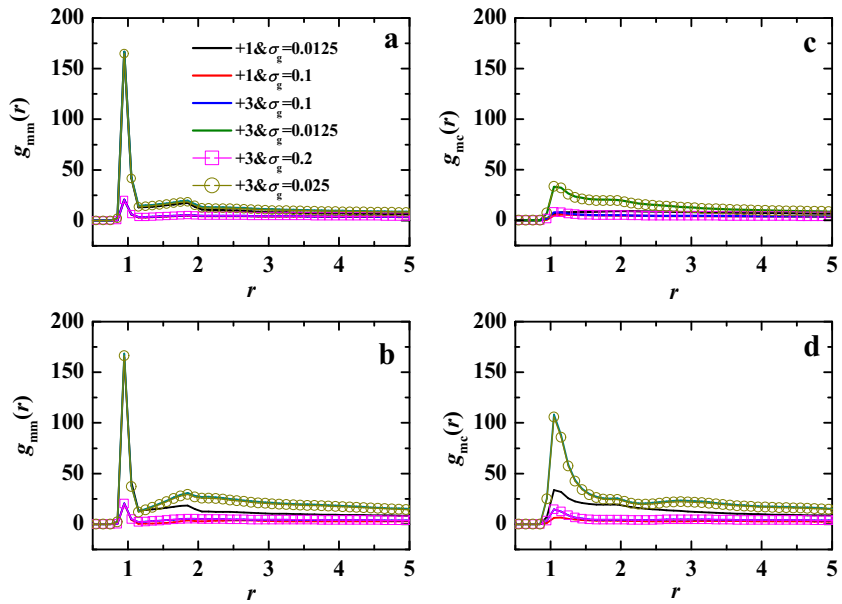

Fig. 11 The pair correlation functions of monomer-monomer $g_{mm}(r)$ and monomer-counterion $g_{mc}(r)$ for the low charge fraction f = 0.1 (upper panels) and high charge fractions f = 1.0 (lower panels). For clarity, the lines represent the ring PE brushes with the chain length N_R = 100 and the open symbols stand for the linear PE brushes with the chain length N_L = 50

are almost consistent with the corresponding ring brushes (blue lines and open squares in Fig. 11).

Because of the importance of the electrostatic bridging mediated by the trivalent counterions, we further calculate the fractions of ψ_{free}, ψ_{NNC}, ψ_{IAB}, and ψ_{IEB} as a function of charge fractions. The calculation method has been demonstrated schematically in Fig. 5. By employing the same cutoff distance $R_c = 2^{1/6}$, the results are shown in Fig. 12. The fractions of free trivalent counterions decrease with the increase of charge fraction (see Fig. 12a) regardless of grafting density and the topology of grafted chains. The increasing local charge density induced by increasing charge fraction facilitates the trivalent counterions to condense onto the chain backbone, and decreases the fraction ψ_{free}, which is consistent with the prediction by Manning theory [48, 49]. For fixed charge fraction, the value of ψ_{free} of low grafting density (σ_g = 0.0125) is larger than that of high grafting density (σ_g = 0.1). And the discrepancy becomes small gradually with the increasing charge fraction. As depicted in Fig. 12b, the fraction of nearest neighbor condensation counterions decreases monotonically with the increase of charge fraction for the high grafting density (filled square in Fig. 12b). However, ψ_{NNC} exhibits a non-monotonic profile as a function of charge fraction for the low grafting density (filled circle in Fig. 12b). We can understand this feature by analyzing the role of the nearest neighbor condensation counterions, that is, the role of counterions in this state is mainly to renormalize the polyion charge to a smaller effective value. The increase of charge fraction firstly makes the trivalent counterions condense onto the chain, represented as the value of ψ_{NNC} increases with the charge fraction firstly, and then the condensed trivalent counterions begin to play the role of bridging due to the decrease of distance of charged monomers, manifested as the decrease of the ψ_{NNC}. The fraction of intra-chain bridging counterions (see Fig. 12c) increases with the increase of charge fraction. Moreover, the extent of the increase of ψ_{IAB} is more obvious for the low grafting density. As shown in Fig. 12d, the fractions of inter-chain bridging counterions increase linearly with the increase of charge fraction. The slopes of the linear profiles are independent on the grafting density. Furthermore, all the fractions trivalent counterions of the 'equivalent' linear brushes (open symbols) are almost identical to the corresponding ring brushes.

Conclusions

In summary, we have performed two sets of MD simulations to provide a systematic analysis of the planar ring PE brushes in good solvent. In the first set, we investigate the effect of grafting density on the surface structures of ring PE brushes. In the mushroom regime, the brush height demonstrates a slight decreasing trend with the increasing grafting density in the presence of trivalent counterions. The height of the brush and the z-component of the radius of gyration R_{gz} scale with the grafting density as $H \sim \sigma_g^{\nu}$ and $R_{gz} \sim \sigma_g^{\nu}$ in the brush regime respectively. And ν is controlled by the charge fraction, chain length, and counterion valence, which indicates that these scaling laws depend on topological features. Based on the distributions of monomers and counterions, the multivalent ion induced collapse of the ring brushes can be observed, especially for the low grafting densities. For the local structuring, the PCF of monomer-monomer is calculated to reveal the electrostatic-correlation-induced order in the

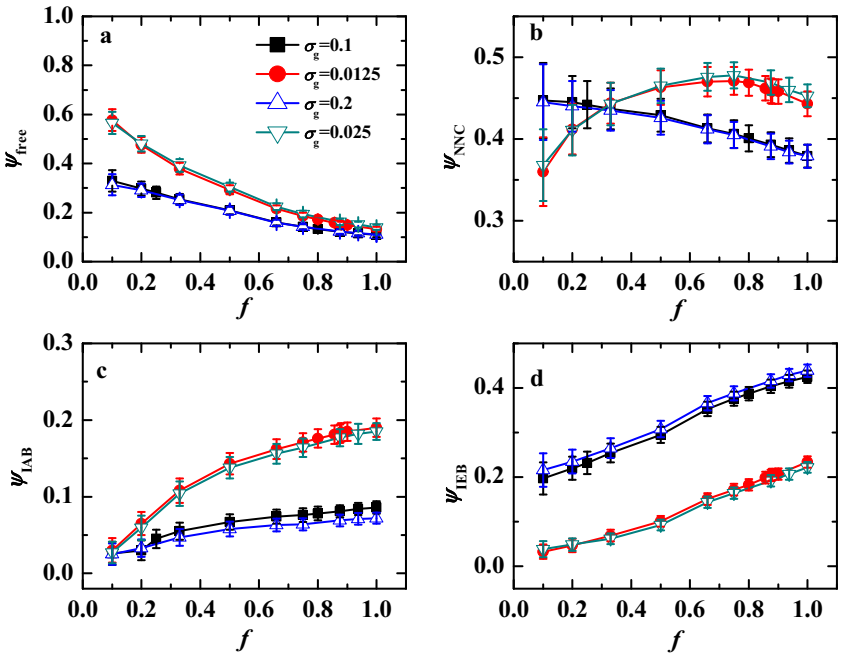

Fig. 12 The fractions of free (**a**), nearest neighbor condensation (**b**), intra-chain bridging (**c**), and inter-chain bridging (**d**) trivalent counterions as a function of charge fraction. The filled symbols correspond to the ring PE brushes with the chain length N_R = 100. The open symbols represent the 'equivalent' linear PE brushes with the chain length N_L = 50

presence of multivalent counterions for the ring PE brushes, even in the good solvent condition.

In the second set, we fix the grafting density, chain length, as well as the counterion valence, and change the charge fractions of the tethered ring PE chains. The effect of charge fraction is examined and compared with those of linear PE brushes. The brush height demonstrates a scaling law relationship with charge fraction as $H \sim f^{\nu}$. As increasing the charge fraction, the brush height increases for the presence of monovalent counterions regardless of grafting density (ν = 0.16, 0.18), remains almost constant for high grafting density with trivalent counterions (ν = 0.01), and decreases for low grafting density with trivalent counterions (ν = − 0.19). The calculations of the PCF of monomer-monomer and monomer-counterions reveal that the increase of charge fraction in the presence of multivalent counterions can induce an ordered morphology for the low grafting densities. Whereas at high grafting densities, the bridging correlation of multivalent counterions is counterbalanced by the excluded volume interaction and electrostatic repulsion of charged segments, which leads the ring PE brush to form homogeneous layer morphology. The findings in this paper may be useful to understand the unique properties of the ring PE brushes for enriching the strategy of surface modification in materials science.

Funding information Financial support was provided by the National Natural Science Foundation of China (NSFC) (Grant Nos. 21674005, 21544007, 21774131) and the Fundamental Research Funds for the Central Universities (Grant No. 3122018L007).

Compliance with ethical standards

Conflict of interest The authors declare that they have no conflict of interest.

References

1. Cohen Stuart MA, Huck WTS, Genzer J, Müller M, Ober C, Stamm M, Sukhorukov GB, Szleifer I, Tsukruk VV, Urban M, Winnik F, Zauscher S, Luzinov I, Minko S (2010). Nat Mater 9:101
2. Das S, Banik M, Chen G, Sinha S, Mukherjee R (2015). Soft Matter 11:8550
3. Kinjo T, Yoshida H, Washizu H (2018). Colloid Polym Sci 296:1
4. Pincus P (1991). Macromolecules 24:2912
5. Motornov M, Tam TK, Pita M, Tokarev I, Katz E, Minko S (2009). Nanotechnology 20:434006
6. Kreer T (2016). Soft Matter 12:3479
7. Benetti EM, Divandari M, Ramakrishna SN, Morgese G, Yan WQ, Trachsel L (2017). Chem Eur J 23:12433
8. Cao DP, Wu JZ (2006). Langmuir 22:2712
9. Zhulina EB, Leermakers FAM, Borisov OV (2016). Macromolecules 49:8758
10. Qiu WJ, Li BH, Wang Q (2018). Soft Matter 14:1887
11. Li L, Yan B, Zhang L, Tian Y, Zeng HB (2015). Chem Commun 51: 15780
12. Wei T, Zhou YY, Zhan WJ, Zhang ZB, Zhu XL, Yu Q, Chen H (2017). Colloids Surf B: Biointerfaces 159:527
13. Morgese G, Trachsel L, Romio M, Divandari M, Ramakrishna SN, Benetti EM (2016). Angew Chem Int Ed 55:15583
14. Morgese G, Trachsel L, Romio M, Divandari M, Ramakrishna SN, Benetti EM (2017). Angew Chem Int Ed 56:2236
15. Divandari M, Morgese G, Trachsel L, Romio M, Dehghani ES, Rosenboom JG, Paradisi C, Zenobi-Wong M, Ramakrishna SN, Benetti EM (2017). Macromolecules 50:7760
16. Morgese G, Shaghasemi BS, Causin V, Zenobi-Wong M, Ramakrishna SN, Reimhult E, Benetti EM (2017). Angew Chem Int Ed 56:4507
17. Erbas A, Paturej J (2015). Soft Matter 11:3139
18. Reith D, Milchev A, Virnau P, Binder K (2011). Europhys Lett 95: 28003
19. Reith D, Milchev A, Virnau P, Binder K (2012). Macromolecules 45:4381
20. Milchev A, Binder K (2013). Macromolecules 46:8724
21. He SZ, Holger M, Su CF, Wu CX (2013). Chin Phys B 22:016101
22. Wan WB, Lv HH, Holger M, Wu CX (2016). Chin Phys B 25: 106101
23. Pei HW, Liu XL, Liu H, Zhu YL, Lu ZY (2017). Phys Chem Chem Phys 19:4710
24. Jones RL, Spontak RJ (1995). J Chem Phys 103:5137
25. Jones RL, Spontak RJ (1994). J Chem Phys 101:5179
26. Gulati HS, Hall CK, Jones RL, Spontak RJ (1996). J Chem Phys 105:7712
27. Goren T, Spencera ND, Crockett R (2014). RSC Adv 4:21497
28. Kremer K, Grest GS (1990). J Chem Phys 92:5057
29. Guptha VS, Hsiao PY (2014). Polymer 55:2900
30. Jackson NE, Brettmann BK, Vishwanath V, Tirrell M, de Pablo JJ (2017). ACS Macro Lett 6:155
31. Hao QH, Xia G, Miao B, Tan HG, Niu XH, Liu LY (2018). Macromolecules 51:8513
32. Yu J, Jackson NE, Xu X, Morgenstern Y, Kaufman Y, Ruths M, de Pablo JJ, Tirrell M (2018). Science 360:1434
33. Frenkel D, Smit B (2002) Understanding molecular simulations. Academic Press, New York
34. Ballenegger V, Arnold A, Cerdà JJ (2009). J Chem Phys 131: 094107
35. Plimpton SJ (1995). J Comput Phys 117:1
36. Cao Q, Zuo C, He H, Li L (2009). Macromol Theory Simul 18:441
37. Cao Q, Zuo C, Li L, He H (2010). Model Simul Mater Sci Eng 18: 075001
38. Csajka FS, Seidel C (2000). Macromolecules 33:2728
39. Farina R, Laugel N, Pincus P, Tirrell M (2013). Soft Matter 9:10458
40. Yu J, Mao J, Yuan G, Satija S, Jiang Z, Chen W, Tirrell M (2016). Macromolecules 49:5609
41. Netz RR, Andelman D (2003). Phys Rep 380:1
42. Alexander S (1977). J Physiol Paris 38:983
43. Milner ST, Witten TA, Cates ME (1988). Macromolecules 21:2610
44. Zhulina EB, Borisov OV, Pryamitsyn VA, Birshtein TM (1991). Macromolecules 24:140
45. Brettmann B, Pincus P, Tirrell M (2017). Macromolecules 50:1225
46. Brettmann BK, Laugel N, Hoffmann N, Pincus P, Tirrell M (2015). J Polym Sci A Polym Chem 54:284
47. Nap RJ, Solveyra EG, Szleifer I (2018). Biomater Sci 6:1048
48. Manning GS (1969). J Chem Phys 51:3249
49. Miao B, Vilgis TA (2012). Macromol Theory Simul 21:582